PROCEEDINGS, 48th Workshop on Geothermal Reservoir Engineering
Stanford University, Stanford, California, February 6-8, 2023
SGP-TR-224

WHOLESCALE - Characterization of conductive fractured zones based on borehole data at San Emidio Geothermal Field, Nevada

Hiroki Sone[1], Oddy Mudatsir[1], Zirou Jin[1], Matt Folsom[2], Gabrielle Ramirez[2], and Kurt L. Feigl[3]

[1]University of Wisconsin-Madison, Geological Engineering, 1415 Engineering Dr., Madison, WI 53706

[2]Ormat Technologies Inc., 6140 Plumas St., Reno, NV 89503

[3]University of Wisconsin-Madison, Department of Geoscience, 1215 W. Dayton St., Madison, WI 53706

E-mail: hsone@wisc.edu

Keywords: WHOLESCALE, San Emidio, Wireline Logging, Mud Logging, Damage Zone

ABSTRACT

Successful heat production from the San Emidio Geothermal Field, Nevada, operated by Ormat Technologies Inc., highlights the existence of conductive pathways for subsurface fluid flow between the injection and production wells. These zones of highly permeable rock formations are identified mainly from drilling records that indicate zones where drilling breaks and lost circulation occur. Interpolation between the high-permeability zones identified in each well allow us to estimate the approximate location and orientation of the first-order planar structure (i.e., fault zone) that constitute the conductive pathway in the subsurface. However, the detailed structural nature of these permeable zones (e.g., fracture distribution, fracture orientation, gouge fill, thickness, and aperture) are still unknown. Such information is essential for conducting a geomechanical analysis to calculate the mechanical response of the permeable zone to injection and production activities. We integrate lithological, structural, petrophysical information from mud, image, and sonic logs to characterize the permeable zones within the reservoir. Lithological boundaries identified in mud logs are used to infer fault planes necessary to match known permeable zones and offsets in lithology. Resistivity image logs reveal abundant natural fractures, potential fault zones (some of which are thicker than tens of feet) that host numerous open fractures and conductive rock units, as well as some potential drilling-induced tensile fractures. Sonic log data also shows low-velocity zones correlated with potential fault zones identified from the image logs. Sonic reflections also reveal the presence and clustering of reflective fracture planes in the vicinity of the borehole. In this paper, we provide a snapshot of work in progress, focusing on the geologic characterization of the permeable zones in the reservoir. Observations show that the most permeable fractures are not always found within the major fault zone structure, suggesting the importance of dissolution/precipitation processes in establishing feed zones. The work presented herein has been funded in part by the Office of Energy Efficiency and Renewable Energy (EERE), U.S. Department of Energy, under Award Number DE-EE0009032.

1. INTRODUCTION

Heat production from geothermal reservoirs in crystalline rocks are facilitated by fluid circulation through pre-existing natural fractures, or through hydraulically propped fractures in the case of enhanced geothermal systems. Locating these fracture systems, as well as understanding their orientation and connectivity, is thus crucial for predicting the efficiency of heat production and understanding their mechanical state within the in-situ stress state.

In the San Emidio geothermal field, Nevada, pathways for fluid circulation has mainly been identified through the observations of drilling events such as drilling breaks and mud circulation losses. The connectivity of these conduits are then also inferred from the local geological structure. However, the properties of these conduits are only known through their well-test analyses (e.g. injectivity) and their physical occurrence has been unknown. For instance, whether fluids circulate through a limited number of key fracture or a network of fractures associated with fault damage zones has not been clear, which may influence the interpretation of their mechanical state and response to changes in stress state.

In 2022, several new wells were drilled in the southern half of the geothermal field from which image logs were collected as well as some basic petrophysical logs. We compare observations of drilling events, occurrence of natural fractures, and feed zones, and highlight their correspondence. Preliminary interpretations suggest that only few fractures are responsible for the majority of the fluid that is planned to be produced from the reservoir.

2. GEOLOGICAL SETTING

The studied geothermal reservoir operated by Ormat Techonologies Inc. is located in the San Emidio desert, northwestern Nevada, United States. The reservoir is located at the eastern margin of the basin created by the north-south striking normal fault system, and the reservoir is situated at a step-over/relay ramp that links normal faults, typical of active geothermal systems in the Basin and Range (Faulds et al., 2011). The orientation of the normal faults are aligned with the present day direction of maximum horizontal stresses inferred from the World Stress Map (Heidbach et al., 2018) and the inversion of focal mechanism from shut-in microseismicities (Jahnke et al., 2022). The reservoir consists of quaternary deposits that fill the basin formed by normal faulting in tertiary tuffaceous sediments, basaltic andesites, and metasediments (Figure 1a). All units encountered in the wells are exposed in the nearby Lake Range to the east of the basin. The shallower units of the reservoir are composed of poorly lithified quaternary sedimentary sequences where the outflow reaching boiling

temperatures is channelized within permeable beach bar deposits and gravels. The deeper units of the reservoir are composed of low porosity volcanic and metamorphic rocks where the fluid transport is likely concentrated in faults and fractures (Folsom et al, 2020).

Figure 1b shows fault planes around the reservoir inferred from the gravity anomalies, magnetotelluric data, and interpolation of depths and locations where lithological changes, drilling events, and feed zones occurred in previously drilled boreholes. The primary fault structure that is relevant to the reservoir near the studied wells are the San Emidio fault (SEF) and the Basin Bounding fault (BBF). Microseismicities observed during the 2016 plant shut down concentrated between these major fault planes (Guo et al., 2016), which may potentially suggest the presence of fractured rock volume between these faults that host fluid circulation. Whether this is a localized damage zone associated with these two faults or not is unclear. Outcrops of basement rocks exposed in the western mountain range show that the tertiary basement rocks can be extensively jointed, sometimes with spacing on the order of centimeters, although the prevalence of such joints at depth is unknown.

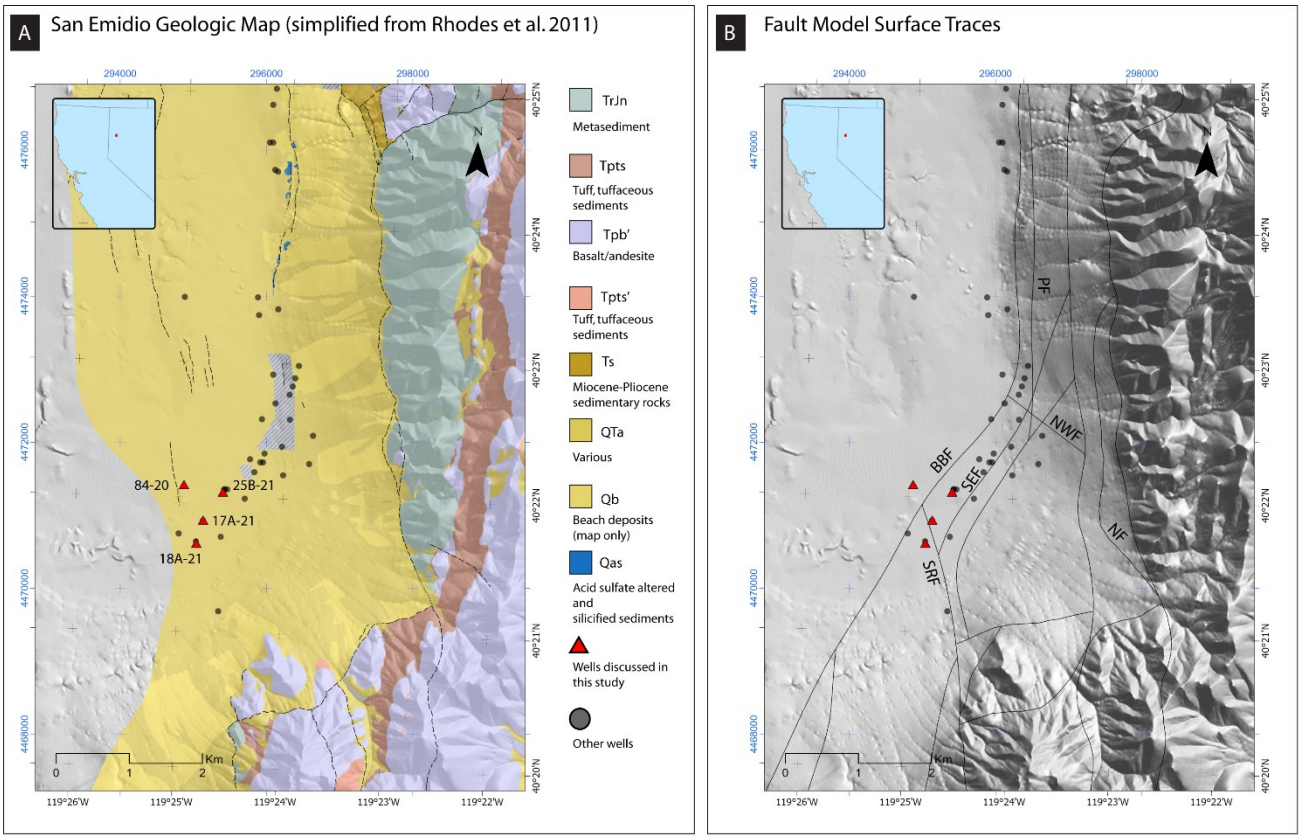

Figure 1: (A) Geological map near San Emidio Geothermal Field modified after Rhodes et al. (2011). (B) The fault structure around the site dominated by a series of northerly striking, westerly dipping normal faults (black lines). SEF: San Emidio fault, BBF: Basin Bounding fault, PF: Piedmont fault, SRF: South Range Front fault, NF: Nightingale fault, NWF: Northwest fault.

3. BOREHOLE DATA

In summer 2022, multiple production and exploratory wells were drilled (Figure 1). Wells 17A-21, 18A-21, 25B-21 were drilled from the hanging wall of San Emidio fault (SEF), reaching 2000~2500 ft depths, and are expected to have penetrate the SEF. Well 84-20 was drilled from the hanging wall of Basin Bounding fault (BBF), reaching 3400 ft depths, and is expected to have penetrated the BBF. In each well, drill cuttings were collected and examined every 10 ft of drilling to observe lithology changes and to construct a lithological column (Figure 2). Standard drilling parameters were also recorded which allowed us to identify drilling breaks and loss circulation zones (Figure 2). In wells 17A-21, 18A-21, 25B-21, resistivity borehole image logs were collected in the open hole intervals covering the main reservoir in the tertiary formations. In well 84-20, an acoustic borehole image log was collected, also in the open hole interval covering the tertiary formations down to the metasediments. In well 17A-21 only, a 3D Far-Field Sonic log (3DFFS) was run which not only captures the direct arrival of the acoustic waves, but also reflections from fractures within the formation. The 3DFFS log provided the compressional and shear wave slowness as well as the depth and orientation information of reflective fractures close to the borehole (Kumar et al., 2019). Following drilling and the collection of downhole logs, the wells were cased with screened liner in their lower sections. They were then tested for permeability using a step-rate test while downhole pressure sensing equipment was hung near zones of inferred permeability (e.g., drilling losses). The precise locations of fluid feed zones were determined using flowing and static pressure, temperature and spinner logs (PTS). In the case of 84-20 this testing was performed under injection. For wells 17A-21, 18A-21 and 25B-21 testing was performed while flowing the wells to a sump.

3.1 Cuttings Analysis and Drilling Record

3.1.1 Lithology and Formation Density from Cuttings Analysis

The lithology sequences encountered in each well roughly followed those expected from the regional geological map compiled by Rhodes et al. (2011). The quaternary alluvium continued to about 400-600 ft depth, followed by a sequence of tertiary claystones before entering the volcanic sequence. Although not identified in the geological map, the presence of the tuffaceous sediments and the andesite appears to be interlayered characterized by multiple appearances of these members, although depth precision of mud logs may not always be precise. Only the deepest well 84-20 reached the metasedimentary Nightingale formation at 2600 ft depth.

Some cuttings were also collected for the purpose of measuring wet densities of the formations. This was done to provide a better constrain on the density of the formations which are used to calculate the vertical stress profile in geomechanical analyses. For tertiary formation cuttings from well 17A-21, the drilling mud was washed off using fresh water, then the excess water was removed from the surface. The weight was then measured on a precision balance and water-saturated volume measured using a helium porosimeter which utilizes the principles of the Boyle's law to calculate sample volume. For quaternary sediments, collecting intact cutting specimens was much more challenging as the formation was likely not fully indurated. Nonetheless, some hand-picked intact fragments from wells 18A-21 and 25B-21 were collected to measure the formation density, with the caveat in mind that these measurements may only serve as an upper limit value. Results are compared with values used to model gravity data in Folsom et al. (2020) in Table 1. The depth trend in the tertiary formations in 17A-21 is also shown later in Figures 6 and 7. The density profile reveals a gently increasing trend, with local perturbations caused by the anomalous presence of some light volcanic sediments.

Table 1: Formation densities inferred in previous geophysical models and measured using cuttings.

Formation	*Mud Log Lithology*	*Gravity Model Density [g/cc] Folsom et al. (2020)*	*Saturated Measured Density [g/cc]*
Qb/QTa	Alluvium	2.02, 2.12	2.28 – 2.41 (upper limit)
Ts	Sand, Clay, Claystones		2.19 – 2.59 (upper limit)
Tpts/Tpts'	Tuffaceous Sediments	2.6	2.39 – 2.60 (mean: 2.42, std dev: 0.08)
Tpb'	Andesite		
Trjn	Metasediments	2.67	n.a.

Table 2: Fault plane depths as inferred from drilling events and testing results. Drilling losses describe intervals where circulating drilling muds were lost to the formation. Tested feed zone intervals follow from the results of flowing PTS logs that identify the precise intervals of permeability. These independent observations often correlate, with some notable differences.

Fault	*Well*	*Drilling Loss Depths [ft kb]*	*Drilling Loss Type*	*Tested Feed Zone Depth [ft kb]*	*Tested Feed Zone Type*
San Emidio Fault	17A-21	2130	Total loss of circulation	2130	Major feed zone
	18A-21	1900	Partial loss	1965	Major feed zone
		1969	Total loss of circulation		
	25B-21	1963	Partial losses	Uncertain depth	Moderate feed zone
		2191	Partial gain of pit volume		
		2372	Partial loss		
Basin Bounding Fault	84-20	2773	Partial losses	2620 – 2750	Moderate feed zone
		2794	Total loss of circulation	2845 – 2900	Minor feed zone
		3047	Partial losses	3152 – 4500	Major feed zone
		3194	Total loss of circulation		
		3353	Total loss of circulation		

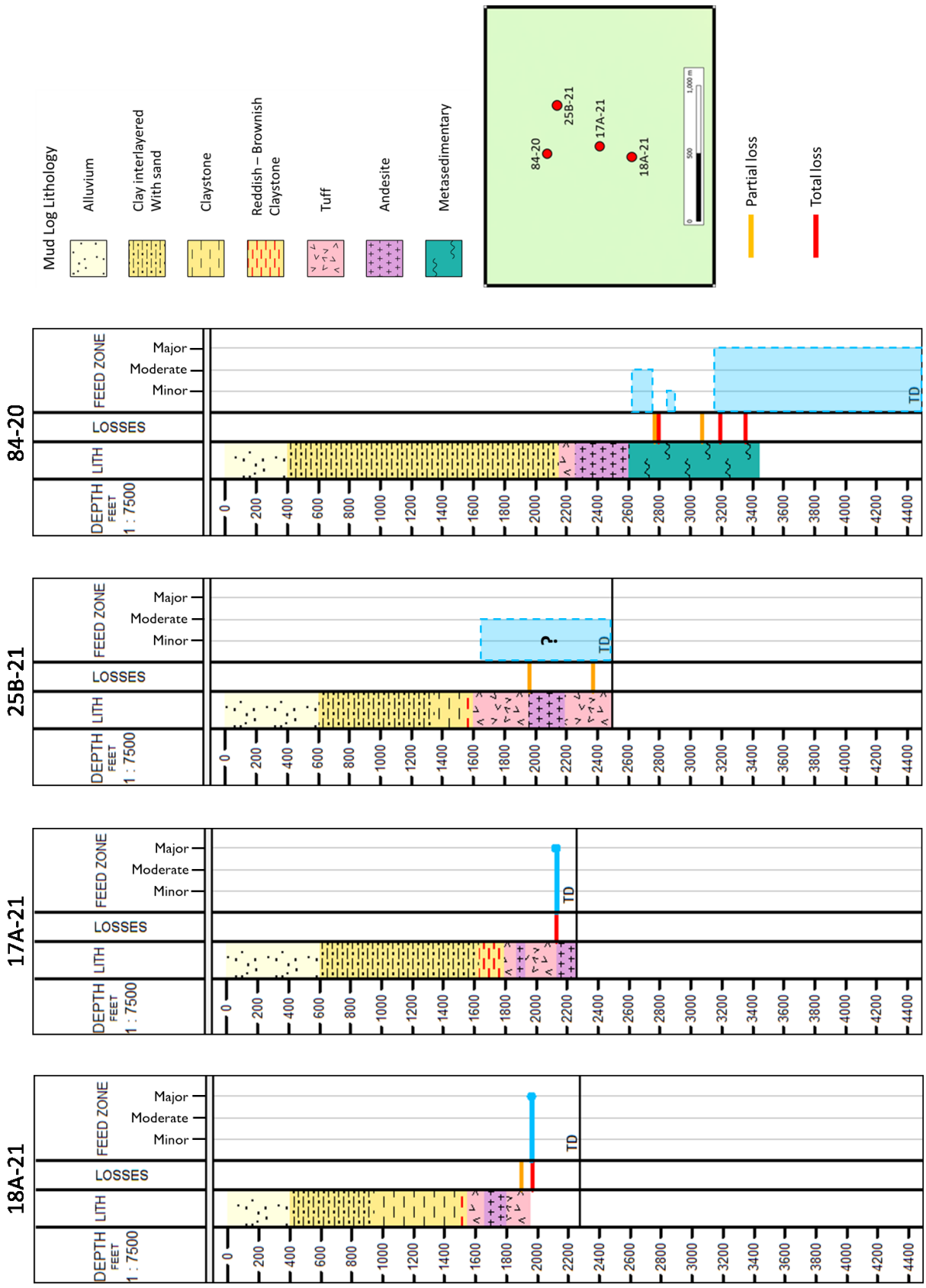

Figure 2: Lithological column inferred from mud log cuttings observations and total/partial loss interval of 18A-21, 17A-21, 25B-21, and 84-20. In 84-20 losses interval occur at metasedimentary interval meanwhile the other three occur at tuff and andesite intervals.

3.1.2 Loss Circulation and Feed Zones from Drilling Records

Circulation losses were encountered at one or more depths in each well where the mud return flow was either partially or totally lost. Circulation losses can be caused by, for instance, the creation of open fractures in the formation when the mud pressure exceeds the minimum principal stress. But in shallow moderately-pressured reservoir like San Emidio, loss zones occur at depths close to high-permeability formations, such as unconsolidated sediments, porous lavas, highly fractured intervals, and fault damage zone (Winn et al., 2021). Circulation losses can also be accompanied by drilling breaks which are recognized as the sudden decrease of weight-on-bit (WOB) and increase of rate-of-penetration (ROP) indicative of the presence of incompetent formations, such as weak porous formations or fractured or brecciated rock masses. Following completion of drilling, image logs are ran in open hole intervals before a screened liner is installed. Well testing is generally performed after the liner is installed.

Depths of loss circulation zones are listed in Table 2 and indicated together with the lithological column in Figure 2. In 18A-21, both partial and total loss circulation occur at 1900 feet and 1969 feet depths, respectively. In 17A-21 total loss circulation occurs at a depth of 2130 feet, which happens at the contact between tuff and andesite. We note, though, that this depth was quite different from the total loss encountered at 1766 ft depth in an adjacent well (17-21) that was drilled previously about 20 ft southwest (along-strike of SE) from well 17A-21. In 25B-21 only partial losses are observed at 1963 feet and 2372 feet, and a partial gain at 2191 ft. In 18A-21, 17A-21, and 25B-21 all losses occur within the tuff or andesite intervals. However, in 84-20 losses occur at deeper intervals within metasedimentary rocks accompanied by frequent occurrence of drilling breaks. There were two partial losses and three total losses in this well. Multiple total losses occur when circulation is recovered over time. Such recovery likely occurs when open fractures are clogged by cuttings as drilling mud is lost into the formation. This may indicate limited aperture, extent, or connectivity of the fractures that were responsible for the total loss zones within the metasediments.

Feed zones are also listed in Table 2 and indicated in Figure 2. In wells 18A-21 and 17A-21, the major feed zone responsible for almost all of the flow rate corresponds to where total loss of circulation was encountered. However, in well 25B-21, no clear the feed zone was identified although two partial loss zones were found. Note that this is in stark contrast with a nearby well (25A-21) that was drilled about 100 ft away to the northeast (along-strike of SEF), which encountered a high permeability fracture causing total loss at 1932 feet depth. In well 84-20, multiple feed zones exist and they are more diffuse spanning over a range of depths. In the moderate and minor feed zones at shallower depths, these feed zones do not correlate with any loss zones although drilling breaks were observed. The major feed zone at the bottom of the well, however, overlap with the two total loss circulation depths and drilling breaks. These observations could be interpreted that the BBF is represented by multiple fault strands rather than a single fault plane.

In summary, wells 18A-21 and 17A-21 clearly intersected a fracture that is responsible for both total loss circulation and production flow rate. Well 25B-21 only intersected minor loss zones that may be contributing to some flow rate. Well 84-20, which is likely the only well that intersected the BBF, encountered numerous loss zones and drilling breaks which is resulting in a rather distributed feed zone within the metasediments.

3.2 Image and Sonic Logs

3.2.1 Image Logs

Image logs highlight heterogeneous features on the borehole wall allowing us to identify planer and linear structures. Resistivity image are scaled so that low-resistivity conductive rocks appear darker. The acoustic image is scaled so that spots with weaker reflections coefficient appear darker. In both type of borehole images, open fluid-filled fractures appear as dark curved or linear features which correspond to natural fractures and drilling-induced tensile fractures (DITFs), respectively. Some examples of natural fractures and DITFs picked in the borehole images are shown in Figure 3. The resistivity images also provide information about the relative resistivity of the formation which reflects the amount of fluid and/or clay minerals in the formation.

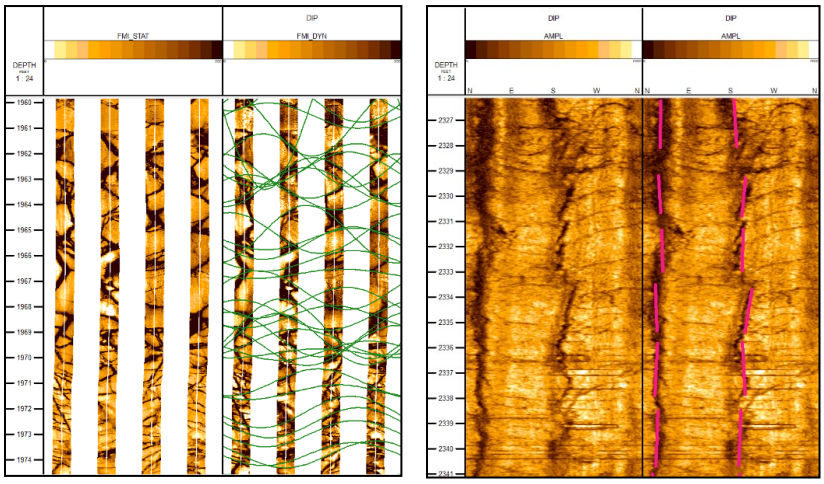

Figure 3: [Left] Example picks of conductive fractures in the resistivity borehole image from well 17A-21. [Right] Example picks of drilling-induced tensile fracture in the acoustic borehole image from well 84-20.

The dip angle, dip azimuth, and fracture density information from all picked fractures are summarized in Figures 4a and 4b. We recognize from the results that the dip azimuth can vary in all directions and the dip angle also varies widely between 20 and 90 degrees. However, the most frequent dip azimuth appears to be in the northwest direction, consistent with the NE-SW striking westward dipping orientation of the SEF and BBF close to the wells. Fractures in the conjugate orientation, dipping southeast, are also found in the tertiary units.

The fracture density also fluctuates along the wells. This does reflect the inherent fluctuation of the fracture density in the formation, but also the fluctuation in our ability to pick fractures from the images. For instance, fractures are difficult to identify when the background formation is also conductive. The borehole also may not retain its original shape due to breakouts and washouts, which leads to low-quality out-of-focus images (Figure 4). Both tend to occur at fault zones because fault rocks can have higher porosity and higher clay-content compared to the surrounding rock mass, and fault rocks are weaker and more prone to compressive rock failures. Taking into account these factors, it is possible to suggest that a typical fault zone architecture (Faulkner et al., 2003) is seen in these image logs where a fault core consisting of fault gouge and fault breccia is surrounded by a damage zone characterized by higher fracture density than the background fracture density in the host rock.

In well 18A-21, there may be a fault core present at around 2060 ft characterized by low resistivity surrounded by high fracture density especially in the footwall. In well 17A-21, a fault core may be present at around 1780 ft with high fracture density above. In well 25B-21, the fault core may be present at 2090 ft with high fracture density above and below. It is interesting to note that these suggested fault cores do not correspond to the loss zones nor the feed zones. It is difficult to make similar inferences based on the acoustic images from well 84-20 because the reflection amplitude relates to the surface condition (i.e. roughness) of the borehole rather than petrophysical properties.

Numerous DITFs were also picked which can give information about the orientation of the horizontal principal stresses and constraints on the horizontal stress magnitudes (Figure 5). The azimuths at which the DITFs occur are consistently in the NNE-SSW direction in all wells which is consistent with the direction of the maximum horizontal stress inferred from the World Stress Map (Heidbach et al., 2018), fault slip indicators (Rhodes, 2011), and the inversion of focal mechanism from shut-in microseismicities (Jahnke et al., 2022). When compared between formations, we find a potential variation in DITF azimuth with depth where the DITF azimuth in the shallow claystone and the deep metasediment appear in the NNE-SSW direction, whereas it is in the NE-SW direction in the tuff and andesite formations.

3.2.2 Sonic Log from Well 17A-21

Because the acoustic velocity of a formation is a function of formation density and rock stiffness, sonic logs provide information about how stiff the formation is given that density variation is typically less than the stiffness variation. The acoustic slowness values are shown in Figure 6, ranging from 60-120 μs/ft and 120-230 μs/ft, for compressional and shear waves, respectively, corresponding to about 2.5-5.1 km/s and 1.3-2.5 km/s velocity, respectively. A notable anomaly is the low velocity seen at 1770-1800 ft depth, which is also where the low resistivity zone is observed. The natural gamma ray also shows a broad peak at this depth. These observations are all consistent with the hypothesis that a relatively compliant, fluid-rich, and clay-rich fault rock exists at this depth interval, surrounded by damaged host rocks.

The 3DFFS log also detected numerous sonic waves reflected from fractures. The fracture orientation information and fracture density distribution recovered from the 3DFFS log is compared with the same information collected independently based on the resistivity image log in Figure 6. Note that fractures were picked manually from resistivity image logs, but were automatically picked using an algorithm from the 3DFFS log (Kumar et al., 2019). The comparison shows that less fractures are detected from the 3DFFS log, especially those fractures with low dip angles owing to the fact that subhorizontal fractures likely do not reflect back acoustic waves to the tool. However, the statistics of the dip direction shown in the Rose diagram and the fracture density distribution agrees quite well. Preferred direction dip directions generally match and peaks and troughs of fracture density also occur at the same depth range, confirming the validity of the interpretations made on the resistivity image logs.

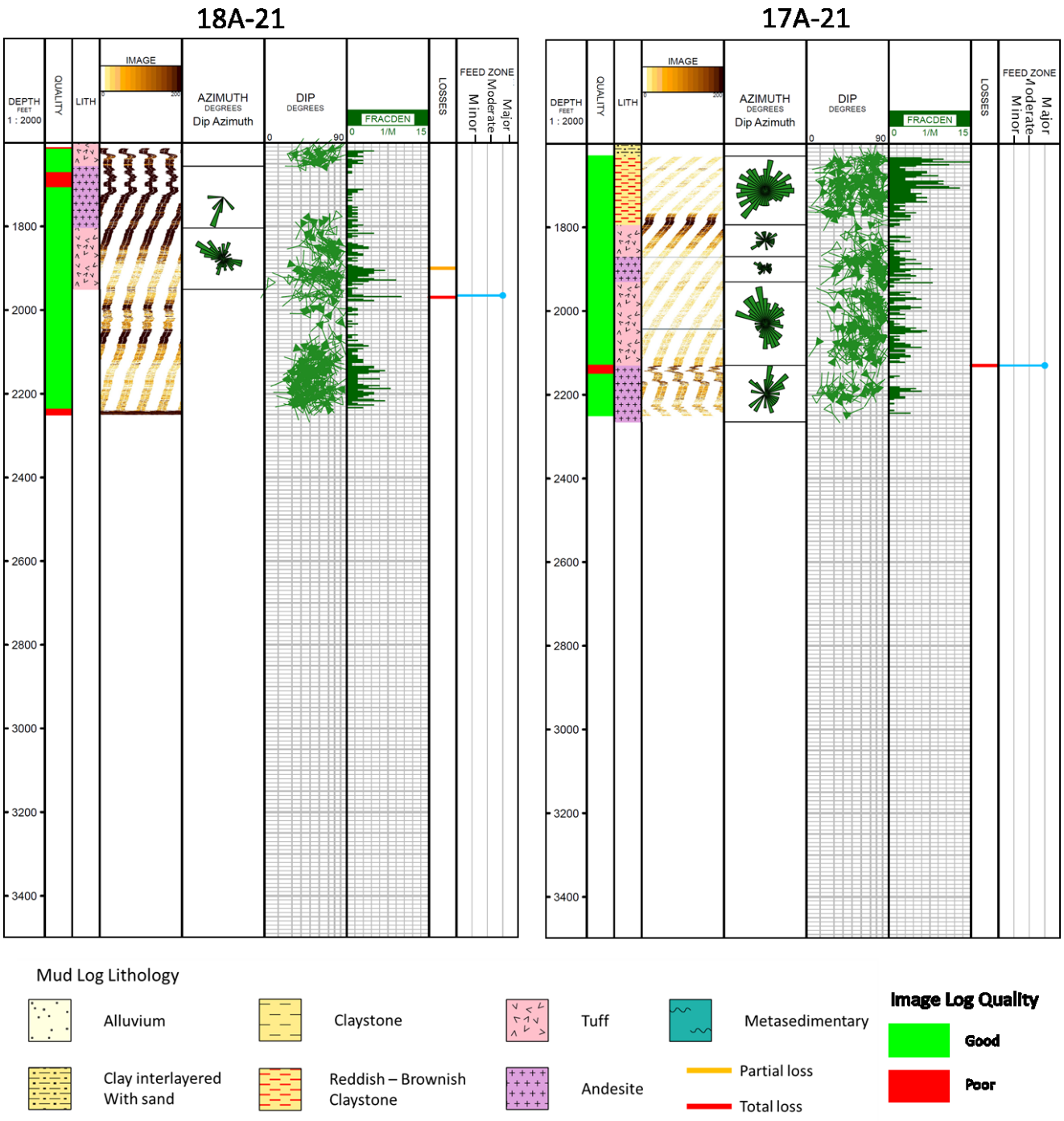

Figure 4a: Resistivity borehole image from wells 18A-21 and 17A-21 along with the orientation and distribution of fractures picked from the image logs.

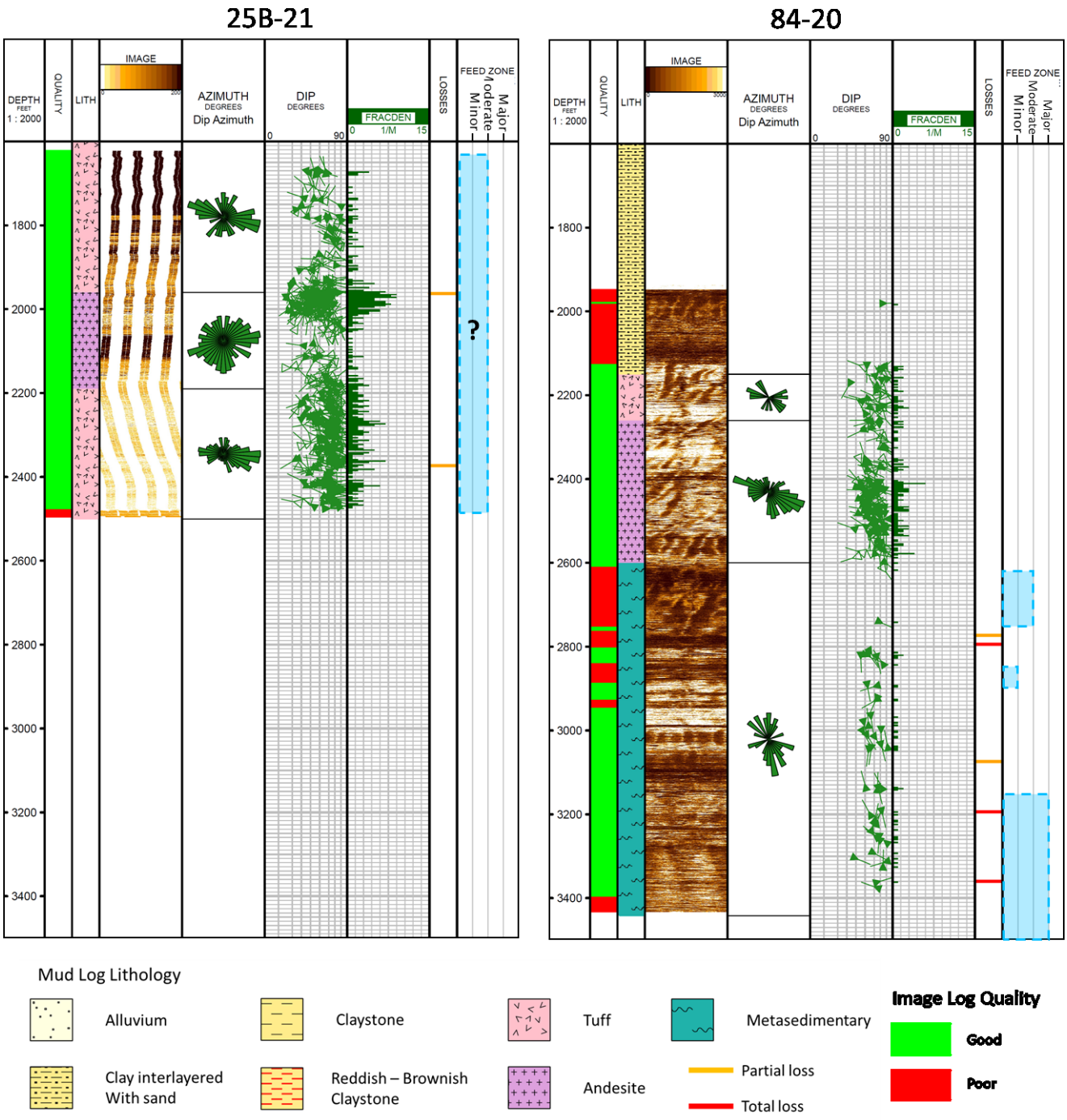

Figure 4b: Resistivity borehole image from well 25B-21 and acoustic borehole image from well 84-20 along with the orientation and distribution of fractures picked from the image logs.

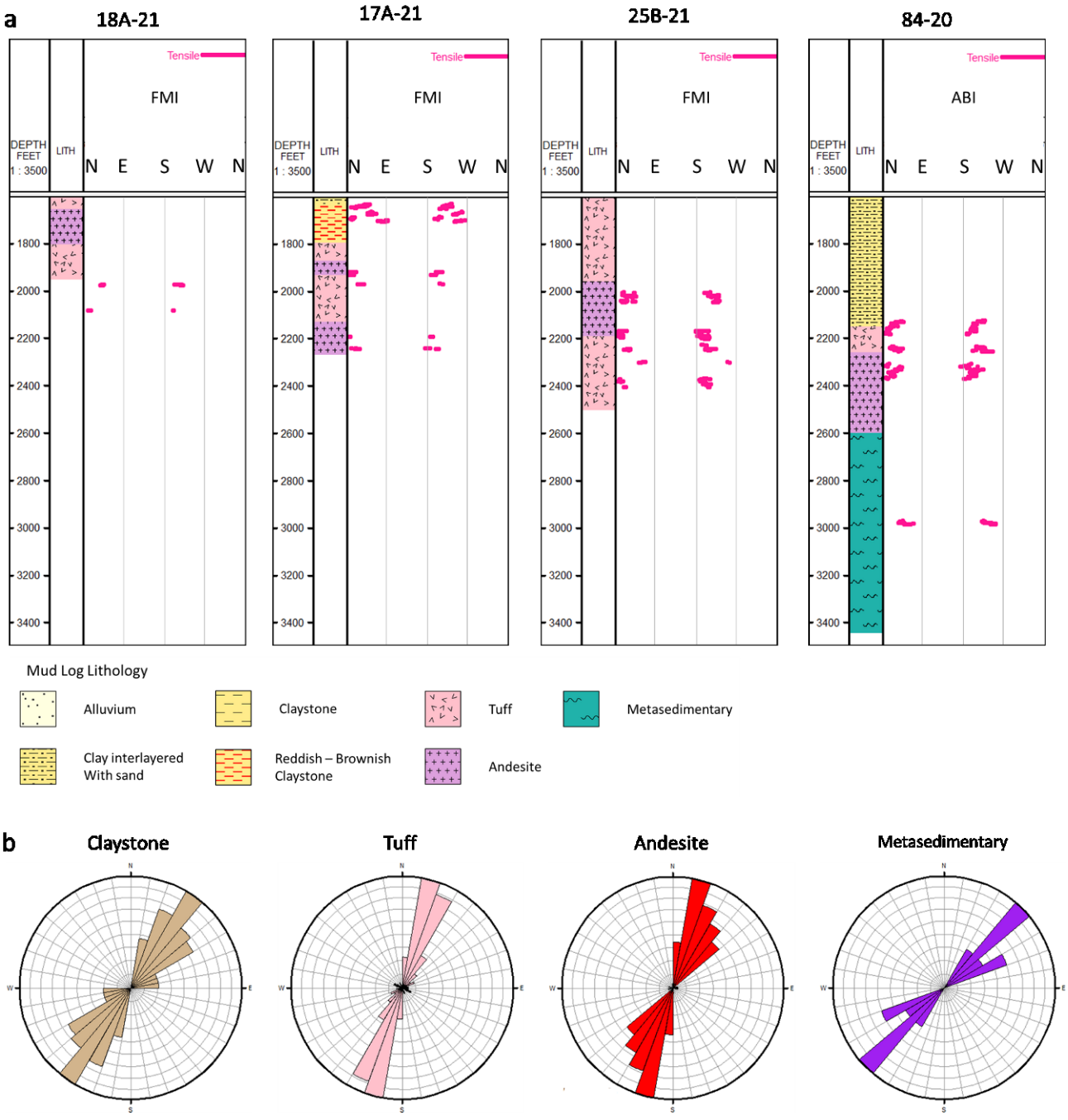

Figure 5: DITF interpretation of all wells. (a) DITF appears in all wells with the azimuth of NE - SW direction. (b) In tuff and andesite intervals DITF is consistent. In claystone and metasedimentary interval, the direction is slightly rotated to the east. The actual azimuth in claystone, tuff-andesite, and metasedimentary are N30E, N10E, and N40E, respectively.

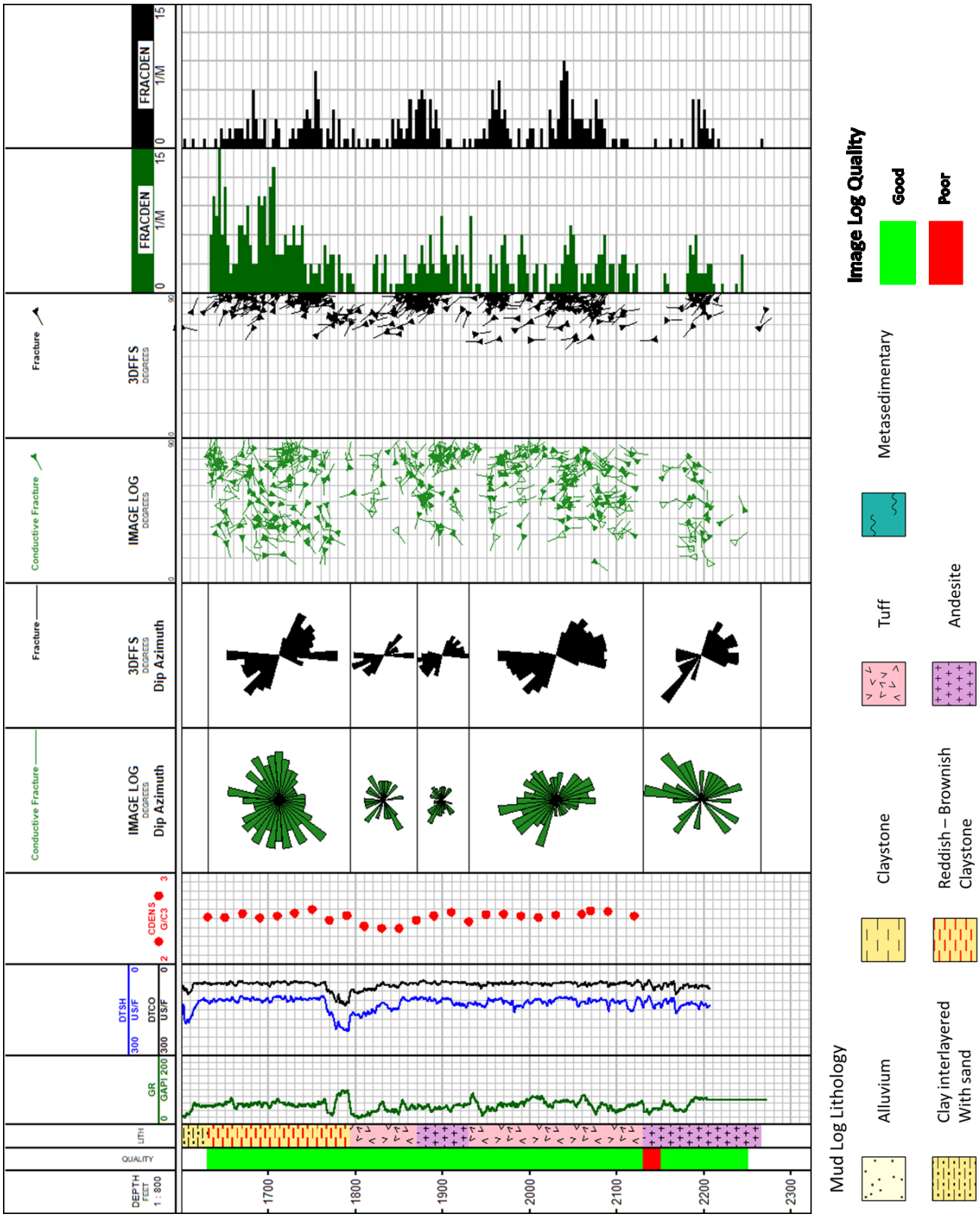

Figure 6: Gamma ray, sonic log data, and comparison of fracture picks from resistivity image log and 3DFFS sonic log data in well 17A-21.

4. PRELIMINARY STRESS ANALYSIS BASED ON BOREHOLE DATA

Given the density information and the occurrence of DITFs in the image logs, we conduct a preliminary stress analysis. The vertical stress profiles were constructed from the formation densities described in Table 1, and pore pressure was assumed to be hydrostatic (Figure 7). We also made an assumption that a leak-off pressure observed in a leak-off test from a nearby well resembles the minimum horizontal stress gradient, which is set at 13.7 MPa/km. Then by setting the frictional coefficient of the formation to be 0.6 (Byerlee, 1978), we can construct a stress polygon describing limits on the horizontal stress magnitude as shown in Figure 7 for a depth of 1973 ft. Because DITFs are observed in these wells, the in-situ stress state must lie along the red line and above the blue line in Figure 8, which suggests a trans-tensional faulting environment. This is consistent with the stress state inferred in Jahnke (2022) based on slip tendency analyses.

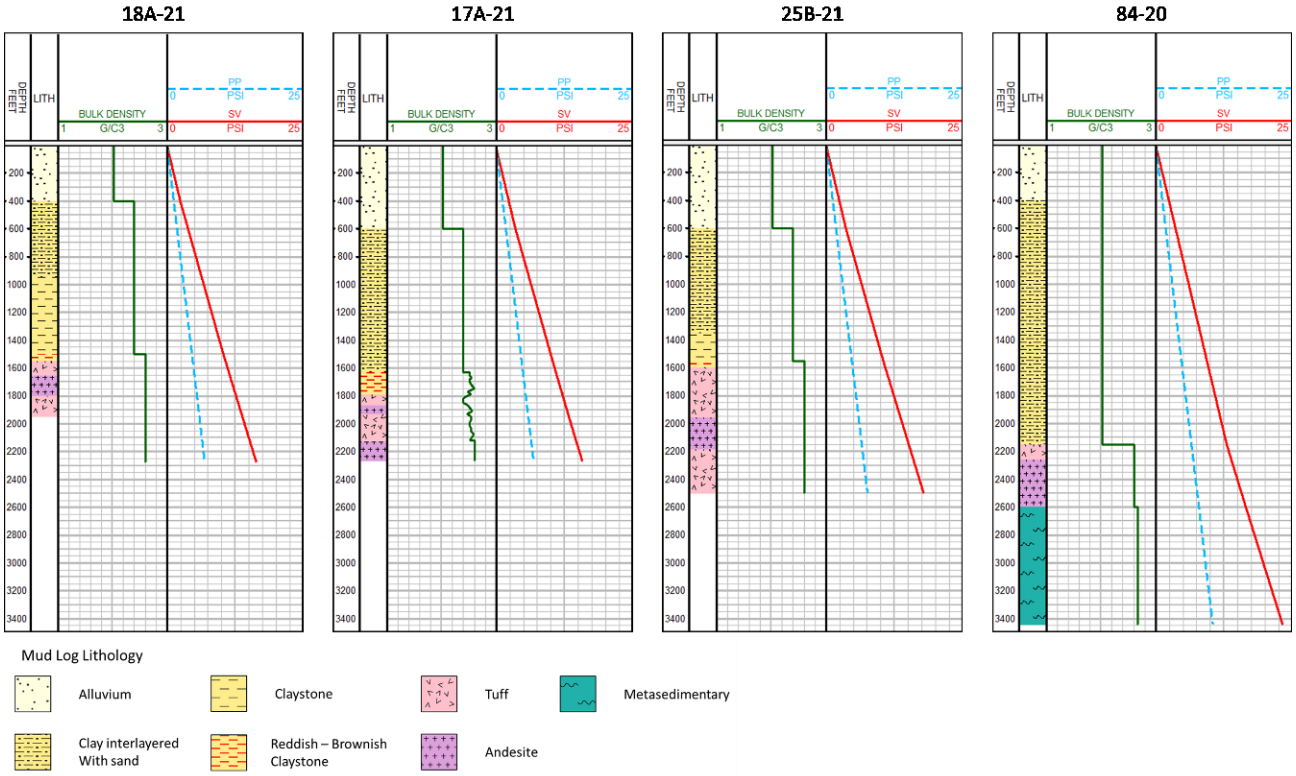

Figure 7: Bulk density profile inferred from the lithological column and also cutting mesurement for well 17A-21. Model density from Folsom et al. (2020).

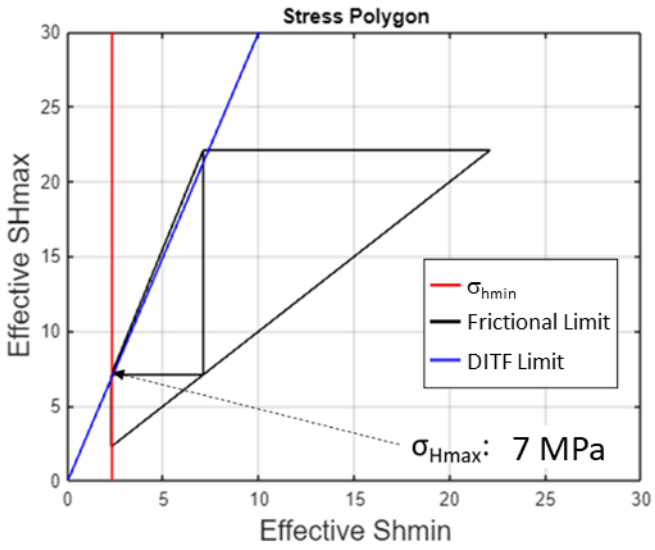

Figure 8: Limits on the magnitude of horizontal stresses at 1973 feet depth from well 18A-21 described in a stress polygon drawn with frictional coefficient 0.6.

5. DISCUSSIONS

5.1 Conductive Pathways for Fluid Flow

As interpreted from the image logs and the sonic logs, it is hypothesized that wells 18A-21, 17A-21, and 25B-21 penetrated a zone possessing a typical architecture of a mature fault zone. The fault core characterized by low resistivity has a thickness on the order of meters and the adjacent damage zone arguably has a width on the order of tens of meters. It is plausible that these faults zones correspond to the San Emidio fault and have accommodated most of the slip along the normal fault and the oblique movement at the stepover.

However, it is also evident that these suggested fault zones are overall not contributing to the hydraulic conductivity in the reservoir. A single feed zone in wells 18A-21 and 17A-21 appears to be responsible for almost all the conductivity despite the abundance of the fractures within the fault damage zones. A zoomed in image of the borehole wall at these feed zones are shown in Figure 9. In well 18A-21, the feed zone consists of only few fractures dipping in the NW direction with aperture potentially more than 10 cm. In well 17A-21, the image quality is poor at the feed zone, but there appears to be large aperture features with no preferred orientation, which may also appear like a vesicular pore structure of a volcanic rock. The origin of these apparently large-aperture features is unknown, but it does not appear to be a structure that accommodated majority of the displacement of the San Emidio fault as they are not associated with a fault damage zone that typically develop with fault displacement along major faults (Faulkner et al., 2011). We also question if it is possible to maintain such large aperture solely due to dilatancy associated with brittle deformation since substantial lithostatic stress exists at in-situ condition. A speculation is that chemical dissolution plays a major role in forming these large apertures features. In well 25B-21, a partial loss zone does coincide with a high-fracture density interval at around 1965 ft depth. But the largest fault zone structure seen around 2100 ft depth and the fractures associated with the fault zone does not appear to be conductive, contrary to the idea that fault damage zones host the largest permeability around fault zones (Lockner et al., 2009).

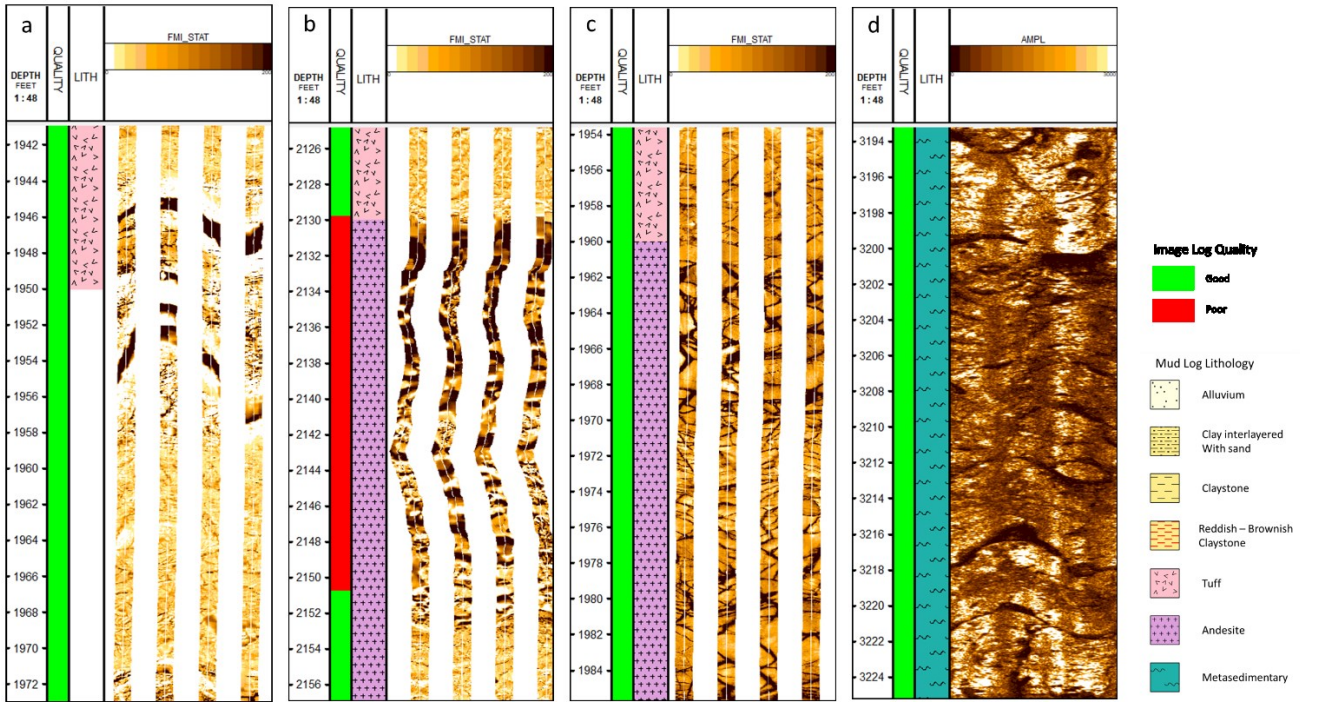

Figure 9: Images log appearances of the loss zones. (a) Total loss zone in 18A-21 suggesting thick conductive sinusoid feature. (b) The total loss zone in 17A-21 show open pore structure. (c) Partial loss zone of 25B-21 coincides with highly fractured andesites. (d) Partial loss zone in 84-20 coincides with a high fracture density interval.

Comparison with feed zones identified in adjacent wells drilled in previous years also highlights the highly variable nature of the conductive fractures in the reservoir. An exploration well 17-21, drilled only 20 ft to the southwest along strike of the SEF, observed total loss of circulation at 1766 ft depth, which is close to the depth of the major fault zone found in well 17A-21. However, no loss of circulation or significant feed zones are observed in well 17A-21 at this depth range, but a few highly-conductive fractures were found at much greater depth with no significant damage zone (Figure 9a). Well 25B-21 also did not encounter any significant feed zone, despite the fact that a previously drilled production well 25A-21 encountered several highly-conductive fractures responsible for total loss of circulation and high permeability, much like what was encountered in wells 18A-21 and 17A-21 from this study. These observations point to the possibility that conductive fractures in the reservoir is highly heterogeneous and may not necessary follow the overall orientation of the largest fault zone structure. The conductive fractures dominating the reservoir fluid flow appears to be meandering within the SEF fault zone and its complex geometry possibly reflects the channelization of fluid flow due to mineral dissolution and precipitation in geothermal systems.

The Basin Bounding fault penetrated by well 84-20 may be presenting a different setting, however. The depth range of the fault zone is unclear due to the lack of petrophysical attributes, but numerous drilling breaks, loss zones, and feed zones are encountered in the metasediment layer. Therefore the entire zone may be hosting a network of conductive fractures contributing to the overall hydraulic conductivity. This may be more consistent with the idea that the highest permeability around fault zones occur in the broad damage zone.

6. CONCLUSION

We find that the relation between faults and fracture occurrences with the actual conductive fluid pathways can vary even between wells that are within few hundred meters away from each other. At times, a single large aperture feature dominates the fluid flow whereas a more distributed zone consisting of a network of fractures can accommodate the fluid flow in other cases. The orientation of the conductive fractures also do not necessarily coincide with the overall orientation of the largest fault structure, which poses a challenge in predicting the depth of feed zones within geothermal systems. The mechanical response of these conductive features may also differ between each other and may motivate a careful discussion about the validity of geomechanical analyses which are primarily based on shear failure criteria, such as the Mohr-Coulomb criterion, to predict the creation and reactivation of fractures.Preliminary analysis of drilling-induced tensile fractures also suggests that the in-situ stress state in the reservoir is largely consistent with the orientation of the regional stress state and faulting environment inferred from past studies.

ACKNOWLEDGEMENTS

We thank Ormat Technologies Inc. for generously sharing data from the San Emidio field, supporting our field activities, and allowing us to publish the data and analysis. We thank Rob Quick, Jeremy Zeveh, and Gabriella Ramirez for sharing space and equipment at the drill site. We thank staffs at the San Emidio Power Plant for allowing us to use their facilities during field work. We are also grateful to John Akerley and Simon Webbison from Ormat Technologies Inc. for reviewing this manuscript and providing valuable insights. The work presented herein has been funded in part by the Office of Energy Efficiency and Renewable Energy (EERE), U.S. Department of Energy, under Award Number DE-EE0009032.

REFERENCES

Byerlee, J. (1978), Friction of rocks, *Pure and Applied Geophysics*, 116, 615-626.

Faulds, J.E., M.F. Coolbaugh, N.H. Hinz, P.H. Cashman, C. Kratt, G. Dering, J. Edwards, B. Mayhew, and H. McLachlan (2011), Assessment of favorable structural settings of geothermal systems in the Great Basin, western USA, Geothermal Resources Council Transactions, 35, 777-784.

Faulkner, D.R., A.C. Lewis, and E.H. Rutter (2003), On the internal structure and mechanics of large strike-slip fault zones: Field observations of the Carboneras fault in southeastern Spain, *Tectonophysics*, 367, 235–251, doi:10.1016/S0040-1951(03)00134-3

Folsom, M., R. Libbey, D. Feucht, I. Warren, and S. Garanzini (2020), Geophysical Observations and Integrated Conceptual Models of the San Emidio Geothermal Field, Nevada, *Proceedings*, *45th Workshop on Geothermal Reservoir Engineering*, Stanford University, Stanford, CA, SGP-TR-216.

Guo, H., C. H. Thurber, B. Heath, M. A. Cardiff, N. E. Lord, I. Warren, and K. L. Feigl (2022), Seismic Analysis of Reservoir Conditions for Inducing Seismicity at the San Emidio Geothermal Field, Nevada, USA. *Abstract*, *2022 SSA Annual Meeting*, Bellevue, WA.

Heidbach, O., M . Rajabi, X. Cui, K. Fuchs, B. Müller, J. Reinecker, K. Reiter, M . Tingay, F. Wenzel, F. Xie, M. O. Ziegler, M .-L. Zoback, and M. D. Zoback (2018), The World Stress Map database release 2016: Crustal stress pattern across scales, *Tectonophysics*, 744, 484-498, doi:10.1016/j.tecto.2018.07.007.

Jahnke, B. J.: Geomechanical Analysis of The Geothermal Reservoir At San Emidio, Nevada And Fracture Toughness Anisotropy Of EGS Collab Testbed Rocks, MS Thesis, University of Wisconsin – Madison, (2022).

Jahnke, B. J., H. Guo, B. Heath, E. Cunningham, C. Sherman, H. Sone, I. Warren, C. Kreemer, C. H. Thurber, K. L. Feigl, and the WHOLESCALE Team (2022), Spatial-Temporal Stress Heterogeneity in the Geothermal Reservoir at San Emidio, Nevada, U.S., *Proceedings*, *47th Workshop on Geothermal Reservoir Engineering*, Stanford University, Stanford, CA, SGP-TR-223.

Kumar, R., N. Bennett, A. Donald, G. Martinez, and E. Velez (2019), 3D Borehole Sonic Imaging for Input to Structural Modeling-A Quantitative Approach, paper presented at *Society of Petroleum Engineers SPE Middle East Oil and Gas Show and Conference*, Manama, Bahrain, http://onepetro.org/SPEMEOS/proceedings-pdf/19MEOS/4-19MEOS/D041S042R001/1144769/spe-194810-ms.pdf/1

Lockner, D. A., H. Tanaka, H. Ito, R. Ikeda, K. Omura, and H. Naka (2009), Geometry of the Nojima Fault at Nojima-Hirabayashi, Japan - I. A Simple Damage Structure Inferred from Borehole Core Permeability, *Pure and Applied Geophysics*, 166, 1649-1667, doi:10.1007/s00024-009-0515-0.

Rhodes, G. T. (2011), Structural Controls of the San Emidio Geothermal System, Northwestern Nevada. MS Thesis, University of Nevada, Reno, http://hdl.handle.net/11714/4011.

Rhodes, G. T., Faulds, J. E., Ramelli, A. R. (2011), Preliminary Geologic Map of the Northern Lake Range, San Emidio Geothermal Area, Washoe County, Nevada, Open-File report, Nevada Bureau of Mines and Geology, 11-11.

Winn, C., Dobson, P., Ulrich, C., Kneafsey, T., Lowry, T., Cesa, Z., Zuza, R., Akerley, J., Delwiche, B., Samuel, A., and Bauer, S.: When, Where, and Why: The Geologic Context of Lost Circulation While Drilling in a Crystalline Geothermal Reservoir, Proceedings, 46th Workshop on Geothermal Reservoir Engineering. Stanford University, Stanford, CA (2022).